LETTER

Surface-Modified Lithium Enabling High-Performance All-Solid-State Lithium Metal Batteries

Hui-Tae Sim, Myung-Keun Oh, Hyo-Jin Kim, Ye-Eun Park, Yun-Sun Cho, Jaeyoung Choi, Seong-Jin Park,* and Dong-Won Kim*

Read Online

ACCESS | Metrics & More | Article Recommendations | Supporting Information

ABSTRACT: Sulfide-based all-solid-state lithium metal batteries (ASSLMBs) are promising next-generation batteries due to their high energy density and safety. However, lithium anodes face challenges like dendrite growth and side reactions at the lithium metal-sulfide electrolyte interface. In this study, we eliminated the resistive native layer on lithium metal and formed a protective layer with high ionic conductivity, mechanical strength, and cohesion by reacting lithium metal with a solution containing nitromethane, dimethoxyethene, and lithium nitrate. The lithium symmetric cell with the surface-modified Li exhibited a high critical current density of 2.8 mA cm^{-2} and stable cycling over 1000 h at 30 °C. The ASSLMB with surface-modified Li anode, Li$_6$PS$_5$Cl electrolyte, and LiNi$_{0.78}$Co$_{0.10}$Mn$_{0.12}$O$_2$ cathode achieved a high discharge capacity (183.2 mAh g^{-1}) and stable cycling for 300 cycles without short-circuit at 0.3 C and 30 °C, which enabled solving the critical challenging issues of Li metal for the development of ASSLMBs.

Legend: Organics, Li$_2$O, Li$_3$N, Li$_2$CO$_3$, LiOH, Others
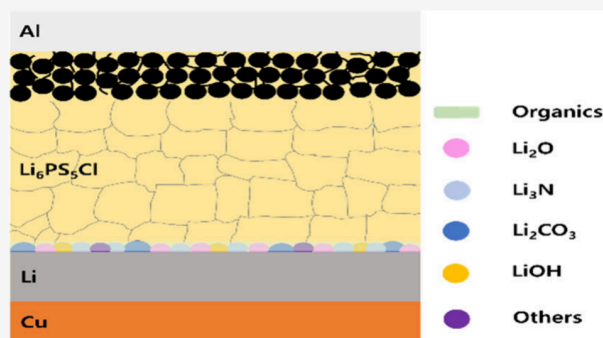
Since the commercialization of lithium-ion batteries (LIBs), they have faced energy density limitations and safety concerns. All-solid-state lithium metal batteries (ASSLMBs) employing lithium metal anodes and solid electrolytes have been considered the most promising next-generation batteries for addressing these issues.[1−4] Among the various solid electrolytes, sulfide electrolytes have attracted considerable attention as the most promising candidates to replace liquid electrolytes because of their ductile properties and high ion conductivity.[5−7] However, the short-circuit caused by lithium dendrite usually occurs during cycling owing to the formation of voids, cracks, and grain boundaries within the solid electrolyte, and side reactions between Li metal and the solid electrolyte also easily occur,[8−13] which are the main obstacles to securing the long cycle life of ASSLMBs. Applying high pressure to the ASSLMBs to improve the interfacial contacts further promoted Li creep and dendrite formation. Moreover, the nonuniform consumption of Li metal and the accumulation of byproducts at the interface during cycling cause a local current to flow, accelerating Li dendrite growth and short-circuiting of the cell. Various strategies have been proposed to address these issues. First, the use of Li-M alloys can suppress Li dendrites by uniformly depositing lithium, and the deposited Li is alloyed to prevent contact

between the Li and the solid electrolyte, thereby mitigating side reactions at the interface to some extent.[14−17] However, the metals used for alloying with Li are expensive, and Li-M alloys have a lower cell voltage than Li metal, resulting in a reduction of the energy density. Second, a solid electrolyte interphase (SEI) layer composed of LiF, Li$_2$O, Li$_3$N, Li$_3$PO$_4$, and organic materials with good mechanical properties, high ionic conductivity, and high interfacial energy with Li metal can efficiently inhibit the formation of Li dendrites, improve the transport of Li ions, and suppress side reactions.[18−21] Since rigid inorganic materials may collapse during the charge–discharge processes, the organic materials in the SEI layer are indispensable for maintaining strong cohesion with the Li anode.[22] Recently, the surface modification of Li metal has allowed Li deposition to be more uniform, resulting in an improvement in the critical current density (CCD) and cycling
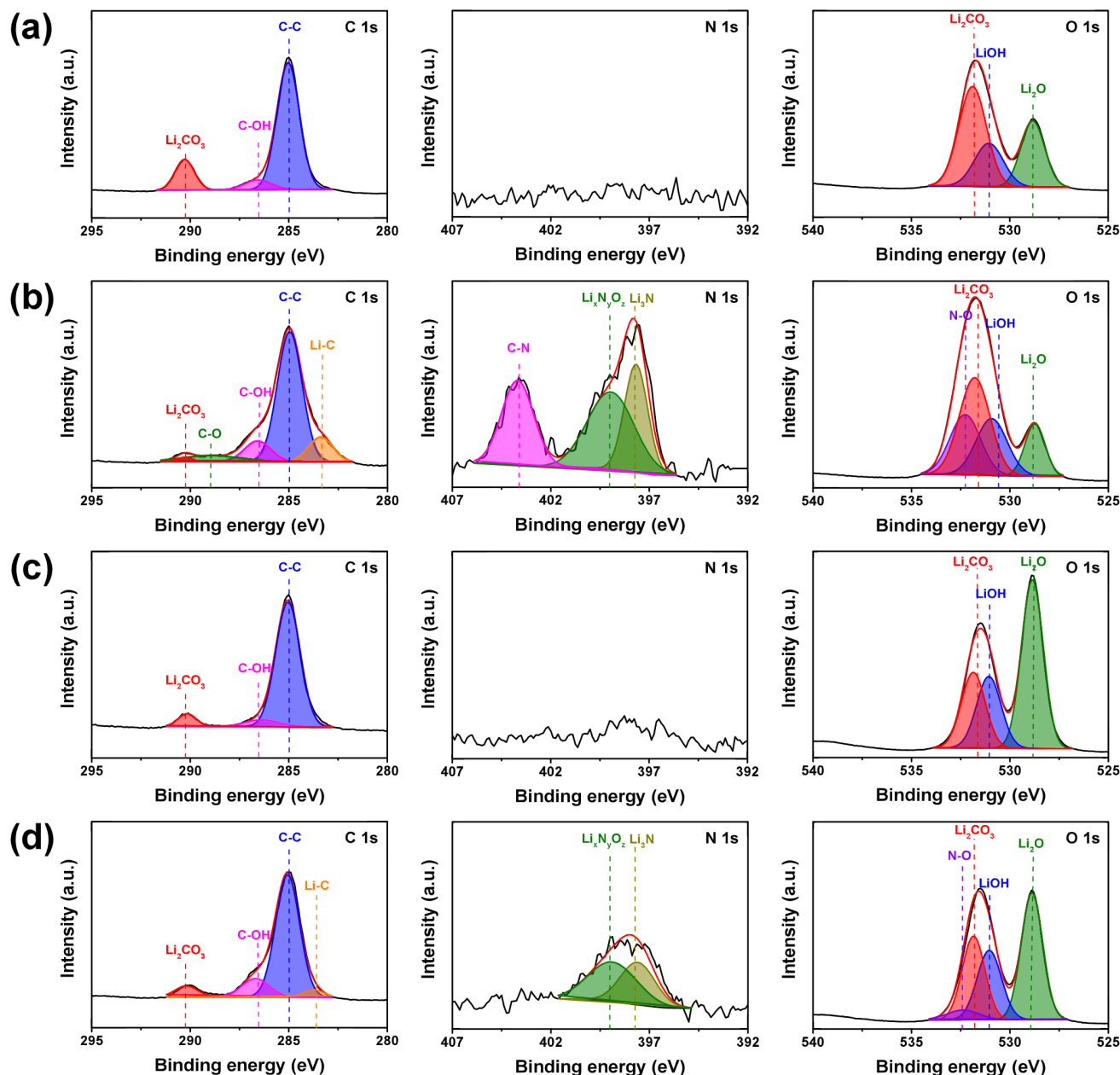
Figure 1. C 1s, N 1s, and O 1s XPS spectra for (a) bare Li, (b) N@Li, (c) DL@Li, and (d) NDL@Li.

stability of lithium metal batteries.[23−25] In this study, we eliminated native resistive materials (LiOH, Li_2O, Li_2CO_3) on the surface of bare Li metal and reconstructed a thin protective layer consisting of Li_2O, Li_3N, and organic materials by reacting the Li metal and a reactive solution containing nitromethane (NM), dimethoxyethane (DME) and lithium nitrate (LNO).[26−28] The surface-modified Li using NM, DME, and LNO (denoted by NDL@Li) promoted the uniform deposition/stripping of Li, prevented the growth of lithium dendrite, exhibited a high CCD, and demonstrated excellent cycling stability without short-circuit.

To investigate the role of the protective layer in stabilizing lithium metal, we analyzed its formation process. To reconstruct the protective layer via chemical reaction with the native layer on the Li metal, bare Li was immersed in a solution containing NM, DME, and LNO (NDL). For comparison, Li was also dipped in NM solvent (denoted by N@Li) and DME-containing LNO (denoted by DL@Li), respectively. The surface morphologies of the obtained Li revealed quite different morphologies (Figure S1). The bare Li metal showed a smooth surface morphology. By contrast, N@ Li had many small particles randomly distributed on the lithium surface. Both DL@Li and NDL@Li exhibit uniform and smooth morphologies. Additional experiments were conducted to analyze the chemical reaction between the reactive solution and Li metal. When Li metal was immersed in the NM, the solvent changed from transparent to light yellow, as shown in Figure S2. This phenomenon was also observed for Li in NDL solution. It is well-known that bare Li metal contains native inorganic materials such as LiOH, Li_2O, and Li_2CO_3 on its surface.[26] To investigate the cause of the color change, commercially available LiOH, Li_2O, and Li_2CO_3 were
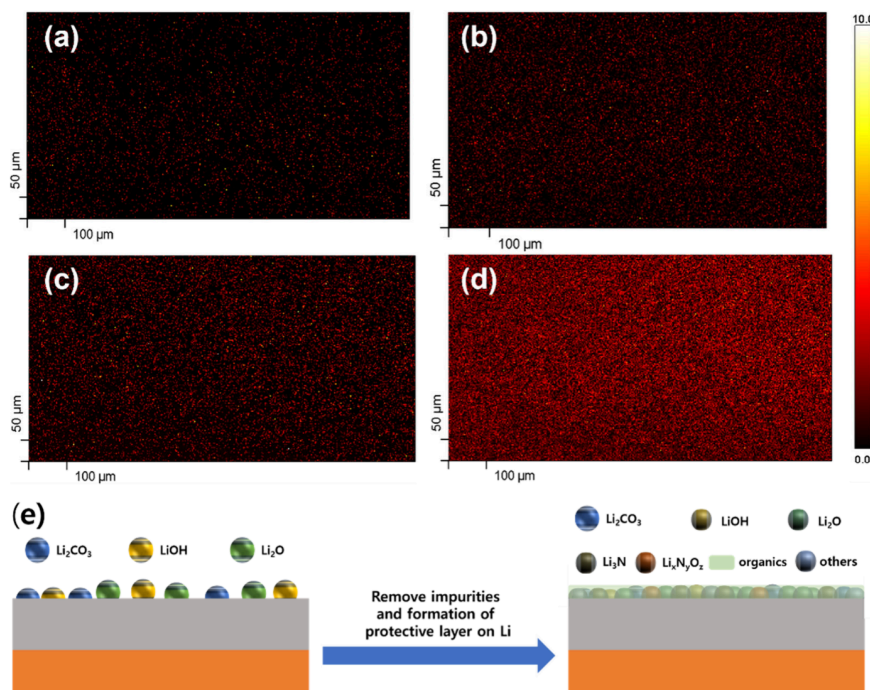
Figure 2. XPS mapping images of (a) LiOH, (b) Li$_2$CO$_3$, (c) Li$_3$N, and (d) Li$_2$O on the NDL@Li. (e) Schematic illustration of the ex-situ formed protective layer for the NDL@Li.

immersed in NM and DME. For simplicity, the solvent containing the Li salt is denoted as Li salt@solvent. As shown in Figure S3, LiOH@NM and Li$_2$O@NM turned yellow. When the solvent was dried, the Li$_2$O and LiOH powders changed to yellow and brown, respectively (Figure S4). The Li salt obtained after drying the solvent was expressed as solvent@Li salt. To confirm whether the NM solvent dissolved the Li salts (LiOH, Li$_2$O) or the reaction products, ^{7}Li NMR spectroscopy was conducted.[29] As presented in Figure S5a and S5b, both LiOH@NM and Li$_2$O@NM exhibited ^{7}Li peaks; whereas, no Li signals were observed in LiOH@DME and Li$_2$O@DME. Additionally, no Li peaks were detected in NM- and DME-containing Li$_2$CO$_3$ (Figure S5c). These results imply that NM dissociates substances containing Li$^+$ ions after reacting with LiOH and Li$_2$O, resulting in color change to yellow in LiOH@NM and Li$_2$O@NM. Organic chemical bonding and inorganic crystal structure were further investigated using Fourier transform infrared (FT-IR) and XRD analysis. In the FT-IR spectrum of NM@LiOH (Figure S6a), a new peak corresponding to R−OH was observed in the range 2700−3500 cm^{-1}, and small peaks attributed to N−O, C−H, and C−N appeared at 1000−1700 cm^{-1}, indicating the formation of organic compounds.[30] In the XRD pattern of NM@LiOH (Figure S6b), additional crystalline peaks corresponding to Li$_3$N are observed at 21.5° and 29.0°,[31] suggesting the production of ion-conductive Li$_3$N from the reaction between NM and LiOH. NM@Li$_2$O also exhibited the characteristic peaks of organic materials in the range of 1000−1700 cm^{-1} (Figure S7a), whereas no additional crystalline peaks were detected in the XRD pattern (Figure S7b).

XPS measurements were performed to investigate the chemical composition of the protective layer on the surface-modified Li. As expected, bare Li contained native inorganic materials such as Li$_2$CO$_3$, LiOH, and Li$_2$O on the surface layer

(Figure 1a).[32] N@Li exhibited C−O, C−OH, and Li−C peaks in the C 1s spectrum,[33] while NO$_2^-$, Li$_x$N$_y$O$_z$ and Li$_3$N peaks were observed in the N 1s spectrum.[34] In addition, an N−O peak was observed with a decrease of Li$_2$O peak intensity in the O 1s region (Figure 1b). DL@Li exhibited peaks similar to those of bare Li; however, it is noticeable that the peak intensity of Li$_2$O was significantly increased (Figure 1c). The peaks appeared in NDL@Li were observed for both N@Li and DL@Li, along with peaks corresponding to C−OH, N−O, Li$_3$N, and Li$_2$O (Figure 1d).

Figure S8 presents the compositional differences among Li, N@Li, DL@Li, and NDL@Li. When using NM-containing solutions (N@Li, NDL@Li), the intensity of the Li$_3$N peak increased significantly. In contrast, the use of LiNO$_3$-containing solutions (DL@Li, NDL@Li) led to a notable increase in the Li$_2$O peak intensity, which is consistent with the earlier observations in Figure 1. This can be explained by the reaction pathways between lithium metal and the NM/LiNO$_3$ (3Li + LiNO$_3$ → 2Li$_2$O + NO, Li + CH$_3$NO$_2$ → Li$_3$N + Li$_x$N$_y$O$_z$ + NO$_2^-$ + organics).

The distribution of the chemical compounds (Li$_2$CO$_3$, Li$_2$O, and Li$_3$N) formed on the Li surface was investigated using XPS mapping, as shown in Figure S9. The XPS mappings of each component for different Li are presented in Figure S10 - S12. Bare Li exhibited a uniform distribution of Li$_2$CO$_3$, Li$_2$O, and LiOH. In contrast, N@Li exhibits a high intensity of Li$_3$N, whereas DL@Li shows a predominance of Li$_2$O. It should be noted that NDL@Li contained large amounts of Li$_3$N and Li$_2$O, resulting in a strong turquoise color, which is a mixture of blue and green (Figure S9d and Figure 2a - 2d). These results are consistent with the XPS results shown in Figure 1. Considering the results discussed above, it can be concluded that Li$_2$O, Li$_3$N, and organic materials were formed on the surface of NDL@Li through the chemical reaction of native
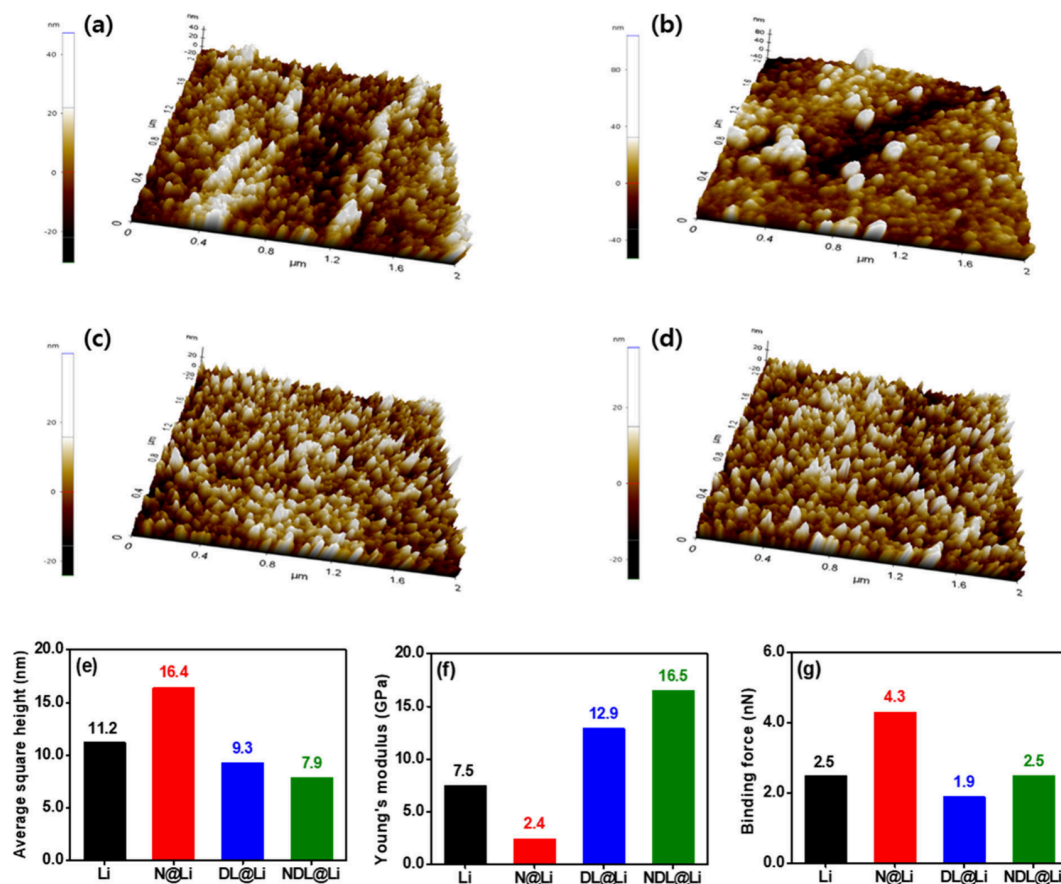
Figure 3. AFM images of (a) bare Li, (b) N@Li, (c) DL@Li, and (d) NDL@Li. Physical properties of different types of Li electrodes obtained from noncontact mode and force−distance measurement (contact mode). (e) Average square height, (f) Young's modulus, and (g) binding force.

materials (Li_2O, and LiOH) on the surface of bare Li and the reactive solution, as schematically illustrated in Figure 2e.

AFM analysis was conducted to evaluate the uniformity and physical properties of the surface layers formed on the different types of Li electrodes. The AFM images and force−distance plots are presented in Figure 3a - 3d and Figure S13, respectively. As shown in Figure 3e, NDL@Li exhibits a lower average square height than the other types of Li, indicating that the surface of NDL@Li is the most uniform and smooth. In contrast, N@Li exhibited the largest average square height, because many particles were unevenly distributed on its surface, as shown in Figure S1b. In terms of the mechanical properties, DL@Li and NDL@Li exhibited higher moduli than bare Li and N@Li (Figure 3f). As previously discussed, both DL@Li and NDL@Li had relatively large amounts of Li_2O compared with bare Li and N@Li. The presence of a large amount of Li_2O in DL@Li and NDL@Li contributes to the enhancement of the modulus, which is effective for suppressing Li dendrite formation and growth during cycling.[35−37] The N@Li exhibited a small portion of Li_2O accompanied by a large amount of organic compounds, yielding the largest binding force.[22] The NDL@Li also contained organic compounds formed by NM, endowing it with a superior binding properties compared to that of DL@Li (Figure 3g).

To investigate the relative thicknesses of the protective layers, we obtained XPS depth profiles of various Li electrodes. In the N 1s spectra, nitrogen-related peaks such as Li_3N and $Li_xN_yO_z$ disappear after 400 s of etching in the N@Li sample,

whereas in NDL@Li, these peaks vanish after 200 s (Figure S14). Similarly, in the O 1s spectra, oxygen-containing species (e.g., Li_2CO_3 and LiOH) are observed up to 400 s in bare Li, disappear after 300 s in DL@Li, and vanish as early as 200 s in NDL@Li (Figure S15). These results confirm that NDL@Li has the thinnest protective layer among the samples, consistent with the enhanced uniformity observed in the AFM analysis (Figure 3d).

The electrochemical impedance spectra of symmetric Li cells employing NDL@Li and solid electrolyte are shown in Figure 4a. The AC impedance spectra of cells with other types of Li electrodes are also presented in Figure S16. The X-axis intercept in the high-frequency represents the bulk resistance of the solid electrolyte (R_{bulk}), whereas the diameter of the semicircle observed in the mid to low-frequency corresponds to the interfacial resistance (R_i).[38] As shown in Figure 4b and 4c, the cells using bare Li and N@Li exhibited a large increase in both R_{bulk} and R_i with time, which can be attributed to side reactions between the solid electrolyte and Li electrodes. By contrast, the cells employing DL@Li and NDL@Li showed relatively stable R_{bulk} and R_i values. This is because of the robust protective layer (e.g., Li_2O with high mechanical strength) that prevents direct contact between the solid electrolyte and Li metal, mitigating deleterious side reactions. To measure the CCD of the symmetric Li cells employing different types of lithium electrodes, the current density for stripping and deposition of lithium was increased from 0.1 to 3.2 mA cm^{-2}. Figure 4d shows the voltage curves of the
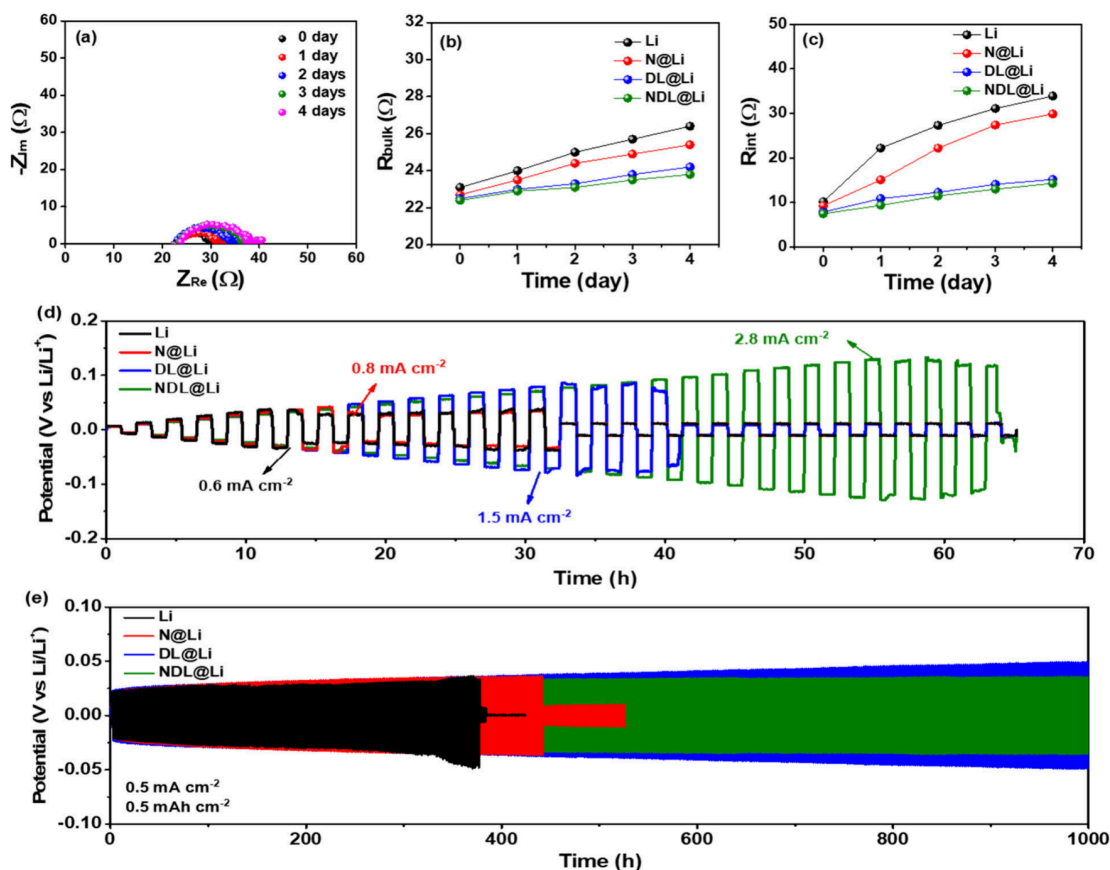
Figure 4. (a) AC impedance spectra of the symmetric NDL@Li/solid electrolyte/NDL@Li cell. (b) Bulk and (c) interfacial resistances of the symmetric Li/solid electrolyte/Li cells with different types of Li. (d) Galvanostatic cycling curves of the Li/solid electrolyte/Li cells with different types of Li at step-increased current densities (the cycle was performed under 1 h deposition and 1 h stripping). (e) Galvanostatic cycling curves of Li/solid electrolyte/Li cells with different types of Li at constant current density of 0.5 mA cm^{-2} and cut-off capacity of 0.5 mAh cm^{-2}.

symmetric Li cells with different Li electrodes as the current density gradually increased. The cell with bare Li exhibits the lowest CCD of 0.6 mA cm^{-2}. When employing surface-modified Li electrodes, the CCD values increased in the following order: N@Li, DL@Li, and NDL@Li. Notably, the cell featuring NDL@Li showed the highest CCD of 2.8 mA cm^{-2}, corresponding to 4.7 times the CCD of the cell with bare Li. The long-term galvanostatic cycling of the symmetric Li cells with different Li electrodes and solid electrolyte was conducted at 0.5 mA cm^{-2} for 1 h during every stripping and deposition cycle. As depicted in Figure 4e, compared with the cells utilizing bare Li and N@Li, the cells employing DL@Li and NDL@Li showed much better cycling stability for up to 1000 h without short circuiting. This is because the DL@Li and NDL@Li electrodes have a protective layer with high mechanical strength that suppresses Li dendrite growth, as discussed in the XPS and AFM results. The cell with NDL@Li exhibited a lower overpotential than the DL@Li cell, which can be ascribed to the enhanced Li$^+$ ion conductivity by the presence of a large amount of Li$_3$N.[31] When cycling the cells at higher current density (1.0 mA cm^{-2}), the cell with bare Li experienced a short-circuit during the formation cycle at lower current density (0.75 mA cm^{-2}), and all cells except for the cell with NDL@Li exhibited a short-circuit when cycling at 1.0 mA cm^{-2}, as shown in Figure S17. These results reveal that NDL@Li with excellent mechanical strength and high ionic

conductivity is a promising electrode for improving the interfacial stability of ASSLBs employing sulfide solid electrolytes. After the repeated cycling of the symmetric Li cells at 0.5 mA cm^{-2}, the cross-sectional morphologies of the Li electrode-solid electrolyte interface in the cells employing bare Li and NDL@Li was investigated. After 350 h, the cell based on bare Li encountered a short-circuit, leading to interfacial collapse, as shown in Figure S18. In contrast, the NDL@Li cell did not exhibit a short-circuit during cycling up to 1000 h and maintained a uniform thickness of lithium after repeated cycling (Figure S19). These results demonstrate that NDL@Li suppresses not only Li dendrite growth but also side reactions at the Li electrode-solid electrolyte interface, leading to significantly enhanced cycling stability compared to bare Li.

ASSLMBs composed of different types of Li anodes, solid electrolytes, and NCM cathodes were assembled, and their cycling performance was evaluated. Figure 5a shows the charge and discharge curves of the cells during the first preconditioning cycle at 0.1 C and 30 °C. The cells delivered the discharge capacities of 180.3 to 183.2 mAh g^{-1}, corresponding to the areal capacities of 3.0 to 3.1 mAh cm^{-2}. After two preconditioning cycles, the cells were cycled at 0.3 C and 30 °C, and their voltage profiles are presented in Figure 5b and S20. The cycling performances are compared in Figure 5c. Except for the cell with the NDL@Li, all the cells showed short-circuiting during the earlier cycles, arising from the
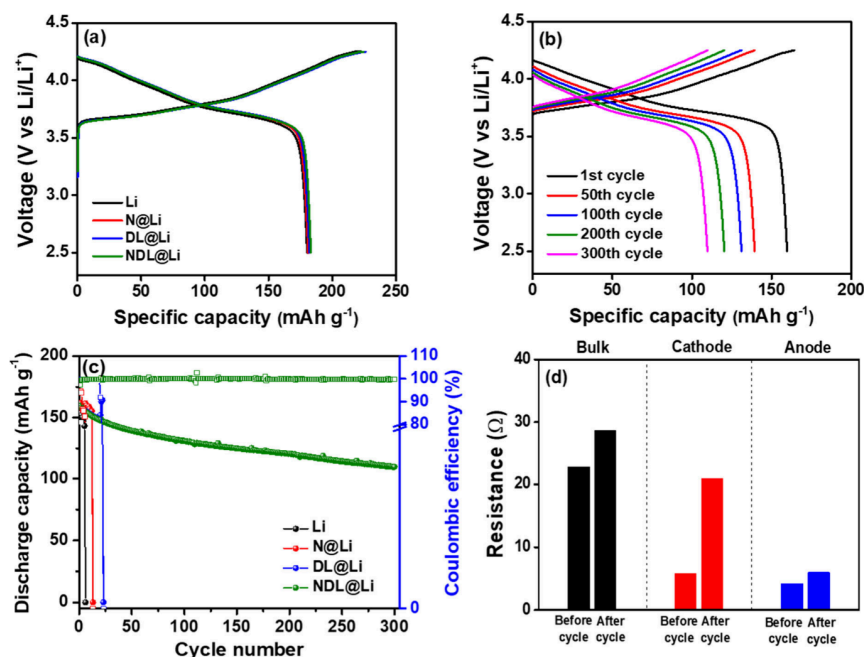
Figure 5. (a) Charge−discharge voltage profiles of the all-solid-state Li/NCM cells during the first conditioning cycle at 0.1 C and 30 °C. (b) Charge−discharge curves of the NDL@Li/solid electrolyte/NCM cell at 0.3 C at 30 °C. (c) Cycling performance of the Li/NCM cells with different types of Li anodes at 0.3 C at 30 °C. (d) Bulk, cathode, and anode resistances of the NDL@Li/solid electrolyte/NCM cell at 30 °C before and after 300 cycles.

growth of lithium dendrites. By contrast, the cell employing the NDL@Li anode exhibited stable charge and discharge cycles without short-circuiting. After 300 cycles, the cell assembled with NDL@Li delivered a discharge capacity of 109.7 mAh g^{-1} at 0.3 C and 30 °C. When comparing the cycling performance of ASSLMBs with Li metal and sulfide-based solid electrolyte reported to date, the cell employing NDL@Li anode (20 μm) and NCM cathode in this work exhibited excellent cycling stability even at the highest areal capacity, as summarized in Table S1. Figure 5d shows the resistances (R_{bulk}, $R_{cathode}$, and R_{anode}) of the ASSLMBs with NDL@Li before and after 300 cycles, which were obtained from the AC impedance in Figure S21.[39] As shown in figure, both the bulk and cathode resistances increased significantly after 300 cycles, whereas the anode resistance maintained similar values after cycling, indicating that the NDL@Li anode had remarkable interfacial stability and few side reactions with the solid electrolyte.

The electrodeposition images after the first formation charge of the cells are shown in Figure S22 and S23, which are obtained by removing solid electrolyte using NMP solvent.[40] Even at low current density (0.3 mA cm^{-2}), Li and N@Li showed a degradation at anode interface, resulting in lithium being deposited in a dendritic form. In contrast, when using DL@Li and NDL@Li, lithium was deposited uniformly. This is because the mechanical properties of Li$_2$O are likely the dominant factor in suppressing dendritic growth and promoting Li deposition beneath the protective layer at low current density. The interfacial morphology between the Li anode and solid electrolyte in the cells with bare Li and NDL@Li was investigated using cross-sectional FIB-SEM analysis. Figure S24a shows the SEM image of the Li-solid electrolyte interface in the cell with bare Li after a short circuit. Minimal lithium remained because of the deleterious side reactions between the Li metal and the sulfide electrolyte during the charge−discharge process. By contrast, the cell employing

NDL@Li retained uniform and thick Li (Figure S24b), because the protective layer on NDL@Li suppressed the side reactions and growth of Li dendrites at the Li anode-solid electrolyte interface.

Our study on the surface-modified Li electrode for ASSLMBs provides insights into strategies for suppressing the growth of lithium dendrites and side reactions of Li metal with sulfide solid electrolytes. NDL@Li, with a uniform, ion-conductive, mechanically strong, and cohesive protective layer, was obtained by the chemical reaction of Li metal with a reactive solution containing nitromethane, dimethoxyethene, and lithium nitrate. Nitromethane reacted with LiOH and Li$_2$O on the surface of the bare Li, and the resulting products (Li$_3$N and organic materials) facilitated Li-ion transport and firmly bound the inorganic materials. Lithium nitrate in dimethoxyethene produces Li$_2$O with high mechanical strength. The use of NDL@Li suppressed Li dendrites and side reactions, thereby preventing Li consumption during cycling. The symmetric Li cell employing NDL@Li exhibited a much higher CCD than bare Li and excellent cycling stability for up to 1000 h at 0.5 mA cm^{-2}. The ASSLMB assembled with NDL@Li anode, sulfide electroelyte, and NCM cathode delivered a high discharge capacity 183.2 mAh g^{-1}, and exhibited good cycling stability without short-circuit over 300 cycles. Consequently, our state-of-the-art work presents a promising strategy for Li anodes to achieve both high energy density and enhanced cycling stability in ASSLMBs. With these significant improvements, the surface modification of bare Li using a reactive solution is proposed as a new strategy for developing next-generation ASSLMBs.

■ **ASSOCIATED CONTENT**

ⓈI Supporting Information

The Supporting Information is available free of charge at https://pubs.acs.org/doi/10.1021/acsenergylett.5c00656.

SEM images of bare lithium and surface modified lithium, photographs of the reactivity between NM solvent and lithium surface materials, ^{7}Li NMR spectra of organic solvents after reaction with lithium surface materials, FT-IR spectra and XRD patterns of LiOH and Li_2O after reaction with NM or DME, Comparative Li 1s XPS peak intensity ratio, XPS mapping images of different types of lithium, AFM plots of different types of lithium, XPS N 1s and O 1s depth profiles of different types of lithium electrodes, AC impedance spectra of the Li symmetric cells as a function of storage time, cycling curves of Li symmetric cells with different types of lithium at 1.0 mA cm^{-2} and 1.0 mAh cm^{-2}, SEM images and EDX mappings after Li symmetric cell test, charge and discharge curves of cells with 3-types lithium except for NDL@Li at 0.3 C, AC impedance spectra of the NDL@Li based cell before and after cycles, SEM images of different types of Li disassembled from the Li/solid electrolyte/NCM cells after formation charging, cross-sectional SEM images of Li/solid electrolyte/NCM cells after cycles (PDF)

■ AUTHOR INFORMATION

Corresponding Authors

Seong-Jin Park − *Next Generation Battery Research Office, SK On Co., Daejeon 34124, South Korea*; Email: SJP@sk.com

Dong-Won Kim − *Department of Chemical Engineering, Hanyang University, Seoul 04763, Korea; Department of Battery Engineering, Hanyang University, Seoul 04763, Korea;* ⊙ orcid.org/0000-0002-1735-0272; Email: dongwonkim@hanyang.ac.kr

Authors

Hui-Tae Sim − *Department of Chemical Engineering, Hanyang University, Seoul 04763, Korea*

Myung-Keun Oh − *Department of Chemical Engineering, Hanyang University, Seoul 04763, Korea*

Hyo-Jin Kim − *Department of Battery Engineering, Hanyang University, Seoul 04763, Korea*

Ye-Eun Park − *Department of Battery Engineering, Hanyang University, Seoul 04763, Korea*

Yun-Sun Cho − *Next Generation Battery Research Office, SK On Co., Daejeon 34124, South Korea*

Jaeyoung Choi − *Inorganics Analysis Division, SK Innovation Co., Ltd, Daejeon 34124, South Korea*

Complete contact information is available at:
https://pubs.acs.org/10.1021/acsenergylett.5c00656

Notes

The authors declare no competing financial interest.

■ ACKNOWLEDGMENTS

■ REFERENCES

(1) Wang, C.; Liang, J.; Zhao, Y.; Zheng, M.; Li, X.; Sun, X. All-Solid-State Lithium Batteries Enabled by Sulfide Electrolytes: From Fundamental Research to Practical Engineering Design. *Energy Environ. Sci.* **2021**, *14*, 2577−2619.

(2) Wu, J.; Liu, S.; Han, F.; Yao, X.; Wang, C. Lithium/Sulfide All-Solid-State Batteries using Sulfide Electrolytes. *Adv. Mater.* **2021**, *33*, 2000751.

(3) Ye, L.; Li, X. A Dynamic Stability Design Strategy for Lithium Metal Solid-State Batteries. *Nature* **2021**, *593*, 218−222.

(4) Zhang, Q.; Cao, D.; Ma, Y.; Natan, A.; Aurora, P.; Zhu, H. Sulfide-Based Solid-State Electrolytes: Synthesis, Stability, and Potential for All-Solid-State Batteries. *Adv. Mater.* **2019**, *31*, 1901131.

(5) Chen, S.; Xie, D.; Liu, G.; Mwizerwa, J. P.; Zhang, Q.; Zhao, Y.; Xu, X.; Yao, X. Sulfide Solid Electrolytes for All-Solid-State Lithium Batteries: Structure, Conductivity, Stability, and Application. *Energy Storage Mater.* **2018**, *14*, 58−74.

(6) Kamaya, N.; Homma, K.; Yamakawa, Y.; Hirayama, M.; Kanno, R.; Yonemura, M.; Kamiyama, T.; Kato, Y.; Hama, S.; Kawamoto, K.; Mitsui, A. A Lithium Superionic Conductor. *Nat. Mater.* **2011**, *10*, 682−686.

(7) Jung, W. D.; Kim, J.-S.; Choi, S.; Kim, S.; Jeon, M.; Jung, H.-G.; Chung, K. Y.; Lee, J.-H.; Kim, B.-K.; Lee, J.-H.; Kim, H. Superionic Halogen-Rich Li-Argyrodites Using In Situ Nanocrystal Nucleation and Rapid Crystal Growth. *Nano Lett.* **2020**, *20*, 2303−2309.

(8) Liu, J.; Yuan, H.; Liu, H.; Zhao, C.-Z.; Lu, Y.; Cheng, X.-B.; Huang, J.-Q.; Zhang, Q. Unlocking the Failure Mechanism of Solid State Lithium Metal Batteries. *Adv. Energy Mater.* **2022**, *12*, 2100748.

(9) Lee, C.; Han, S. Y.; Lewis, J. A.; Shetty, P. P.; Yeh, D.; Liu, Y.; Klein, E.; Lee, H.-W.; McDowell, M. T. Stack Pressure Measurements to Probe the Evolution of the Lithium-Solid-State Electrolyte Interface. *ACS Energy Lett.* **2021**, *6*, 3261.

(10) Ning, Z.; Jolly, D. S.; Li, G.; De Meyere, R.; Pu, S. D.; Chen, Y.; Kasemchainan, J.; Ihli, J.; Gong, C.; Liu, B.; Melvin, D. L. R.; Bonnin, A.; Magdysyuk, O.; Adamson, P.; Hartley, G. O.; Monroe, C. W.; Marrow, T. J.; Bruce, P. G. Visualizing Plating-Induced Cracking in Lithium-Anode Solid-Electrolyte Cells. *Nat. Mater.* **2021**, *20*, 1121−1129.

(11) Lewis, J. A.; Cortes, F. J. Q.; Liu, Y.; Miers, J. C.; Verma, A.; Vishnugopi, B. S.; Tippens, J.; Prakash, D.; Marchese, T. S.; Han, S. Y.; Lee, C.; Shetty, P. P.; Lee, H.-W.; Shevchenko, P.; De Carlo, F.; Saldana, C.; Mukherjee, P. P.; McDowell, M. T. Linking Void and Interphase Evolution to Electrochemistry in Solid-State Batteries Using Operando X-Ray Tomography. *Nat. Mater.* **2021**, *20*, 503−510.

(12) Kasemchainan, J.; Zekoll, S.; Jolly, D. S.; Ning, Z.; Hartley, G. O.; Marrow, J.; Bruce, P. G. Critical Stripping Current Leads to Dendrite Formation on Plating in Lithium Anode Solid-Electrolyte Cells. *Nat. Mater.* **2019**, *18*, 1105−1111.

(13) Ning, Z.; Li, G.; Melvin, D. L. R.; Chen, Y.; Bu, J.; Jolly, D. S.; Liu, J.; Hu, B.; Gao, X.; Perera, J.; Gong, C.; Pu, S. D.; Zhang, S.; Liu, B.; Hartley, G. O.; Bodey, A. J.; Todd, R. I.; Grant, P. S.; Armstrong, D. E. J.; Marrow, T. J.; Monroe, C. W.; Bruce, P. G. Dendrite Initiation and Propagation in Lithium Metal Solid-State Batteries. *Nature* **2023**, *618*, 287−293.

(14) Pan, H.; Zhang, M.; Cheng, Z.; Jiang, H.; Yang, J.; Wang, P.; He, P.; Zhou, H. Carbon-Free and Binder-Free Li-Al Alloy Anode Enabling an All-Solid-State Li-S Battery with High Energy and Stability. *Sci. Adv.* **2022**, *8*, No. eabn4372.

(15) Lim, H.; Jun, S.; Song, Y. B.; Bae, H.; Kim, J. H.; Jung, Y. S. Operando Electrochemical Pressiometry Probing Interfacial Evolution of Electrodeposited Thin Lithium Metal Anodes for All-Solid-State Batteries. *Energy Storage Mater.* **2022**, *50*, 543−553.

(16) Aspinall, J.; Sada, K.; Guo, H.; Kotadkadi, S.; Narayanan, S.; Chart, Y.; Jagger, B.; Milan, E.; Brassart, L.; Armstrong, D.; Pasta, M. The Impact of Magnesium Content on Lithium-Magnesium Alloy Electrode Performance with Argyrodite Solid Electrolyte. *Nat. Commun.* **2024**, *15*, 4511.

(17) Liao, Y.-L.; Hu, J.-K.; Fu, Z.-H.; Zhao, C.-Z.; Lu, Y.; Li, S.; Yang, S.-J.; Sun, S.; Wang, X.-L.; Liu, J.; Huang, J.-Q.; Yuan, H. Integrated Interface Configuration by In-Situ Interface Chemistry Enabling Uniform Lithium Deposition in All-Solid-State Lithium Metal Batteries. *J. Energy Chem.* **2023**, *80*, 458−465.

(18) Su, H.; Liu, Y.; Zhong, Y.; Li, J.; Wang, X.; Xia, X.; Gu, C.; Tu, J. Stabilizing the Interphase Between Li and Argyrodite Electrolyte

through Synergistic Phosphating Process for All-Solid-State Lithium Batteries. *Nano Energy* **2022**, *96*, 107104.

(19) Wu, Y.; Sun, X.; Li, R.; Wang, C.; Song, D.; Yang, Z.; Gao, J.; Zhang, Y.; Ohsaka, T.; Matsumoto, F.; Zhao, F.; Wu, J. In Situ Construction of Trinity Artificial Protective Layer Between Lithium Metal and Sulfide Solid Electrolyte Interface. *Electrochem. Commun.* **2022**, *142*, 107377.

(20) Wu, M.; Li, M.; Jin, Y.; Chang, X.; Zhao, X.; Gu, Z.; Liu, G.; Yao, X. In Situ Formed LiF-Li$_3$N Interface Layer Enables Ultra-Stable Sulfide Electrolyte-Based All-Solid-State Lithium Batteries. *J. Energy Chem.* **2023**, *79*, 272.

(21) Liu, Y.; Lin, D.; Li, Y.; Chen, G.; Pei, A.; Nix, O.; Li, Y.; Cui, Y. Solubility-Mediated Sustained Release Enabling Nitrate Additive in Carbonate Electrolytes for Stable Lithium Metal Anode. *Nat. Commun.* **2018**, *9*, 3656.

(22) Jagger, B.; Pasta, M. Solid Electrolyte Interphases in Lithium Metal Batteries. *Joule* **2023**, *7*, 2228−2244.

(23) Liang, Y.; Shen, C.; Liu, H.; Wang, C.; Li, D.; Zhao, X.; Fan, L.-Z. Tailoring Conversion-Reaction-Induced Alloy Interlayer for Dendrite-Free Sulfide-Based All-Solid-State Lithium-Metal Battery. *Adv. Sci.* **2023**, *10*, 2300985.

(24) Xie, Y.; Huang, Y.; Zhang, Y.; Wu, T.; Liu, S.; Sun, M.; Lee, B.; Lin, Z.; Chen, H.; Dai, P.; Huang, Z.; Yang, J.; Shi, C.; Wu, D.; Huang, L.; Hua, Y.; Wang, C.; Sun, S. Surface Modification Using Heptafluorobutyric Acid to Produce Highly Stable Li Metal Anodes. *Nat. Commun.* **2023**, *14*, 2883.

(25) Shen, X.; Zhang, R.; Chen, X.; Cheng, X.-B.; Li, X.; Zhang, Q. The Failure of Solid Electrolyte Interphase on Li Metal Anode: Structural Uniformity or Mechanical Strength? *Adv. Energy Mater.* **2020**, *10*, 1903645.

(26) Kanamura, K. Multiscale Researches on Lithium Ion and Lithium Metal Batteries. *Electrochemistry* **2022**, *90*, 101001.

(27) Jin, D.; Roh, Y.; Jo, T.; Ryou, M.-H.; Lee, H.; Lee, Y. M. Robust Cycling of Ultrathin Li Metal Enabled by Nitrate-Preplanted Li Powder Composite. *Adv. Energy Mater.* **2021**, *11*, 2003769.

(28) Hwang, J.-Y.; Park, S.-J.; Yoon, C. S.; Sun, Y.-K. Customizing a Li-Metal Battery That Survives Practical Operating Conditions for Electric Vehicle Applications. *Energy Environ. Sci.* **2019**, *12*, 2174−2184.

(29) Hu, J. Z.; Jaegers, N. R.; Hu, M. Y.; Mueller, K. T. In Situ and Ex Situ NMR for Battery Research. *J. Phys.: Condens. Matter* **2018**, *30*, 463001.

(30) Pal, C.; Hazra, A.; Ghosh, P. N.; Kshirsagar, R. J. High-Resolution Fourier Transform Infrared Spectrum and Vibration-Rotation Analysis of the B-Type 1584 cm^{-1} Band of Nitromethane. *J. Mol. Struct.* **1997**, *407*, 165−170.

(31) Li, W.; Wu, G.; Araujo, C. M.; Scheicher, R. H.; Blomqvist, A.; Ahuja, R.; Xiong, Z.; Feng, Y.; Chen, P. Li$^+$ Ion Conductivity and Diffusion Mechanism in α-Li$_3$N and β-Li$_3$N. *Energy Environ. Sci.* **2010**, *3*, 1524−1530.

(32) Zhao, B.; Li, J.; Guillaume, M.; Dendooven, J.; Detavernier, C. In Vacuo XPS Investigation of Surface Engineering for Lithium Metal Anodes with Plasma Treatment. *J. Energy Chem.* **2022**, *66*, 295−305.

(33) Ma, Q.; Tong, B.; Fang, Z.; Qi, X.; Feng, W.; Nie, J.; Hu, Y.-S.; Li, H.; Huang, X.; Chen, L.; Zhou, Z. Impact of Anionic Structure of Lithium Salt on the Cycling Stability of Lithium-Metal Anode in Li-S Batteries. *J. Electrochem. Soc.* **2016**, *163*, A1776−A1783.

(34) Lin, X.-D.; Gu, Y.; Shen, X.-R.; Wang, W.-W.; Hong, Y.-H.; Wu, Q.-H.; Zhou, Z.-Y.; Wu, D.-Y.; Chang, J.-K.; Zheng, M.-S.; Mao, B.-W.; Dong, Q.-F. An Oxygen-Blocking Oriented Multifunctional Solid-Electrolyte Interphase as a Protective Layer for a Lithium Metal Anode in Lithium-Oxygen Batteries. *Energy Environ. Sci.* **2021**, *14*, 1439−1448.

(35) Hull, S.; Farley, T. W. D.; Hayes, W.; Hutchings, M. T. The Elastic Properties of Lithium Oxide and Their Variation with Temperature. *J. Nucl. Mater.* **1988**, *160*, 125−134.

(36) Masias, A.; Felten, N.; Garcia-Mendez, R.; Wolfenstine, J.; Sakamoto, J. Elastic, Plastic, and Creep Mechanical Properties of Lithium Metal. *J. Mater. Sci.* **2019**, *54*, 2585−2600.

(37) Hobold, G. M.; Wang, C.; Steinberg, K.; Li, Y.; Gallant, B. M. High Lithium Oxide Prevalence in the Lithium Solid-Electrolyte Interphase for High Coulombic Efficiency. *Nat. Energy* **2024**, *9*, 580−591.

(38) Jiang, T.; He, P.; Liang, Y.; Fan, L.-Z. All-Dry Synthesis of Self-Supporting Thin Li$_{10}$GeP$_2$S$_{12}$ Membrane and Interface Engineering for Solid-State Lithium Metal Batteries. *J. Chem. Eng.* **2021**, *421*, 129965.

(39) Choi, H. J.; Kang, D. W.; Park, J.-W.; Park, J.-H.; Lee, Y.-J.; Ha, Y.-C.; Lee, S.-M.; Yoon, S. Y.; Kim, B. G. In Situ Formed Ag-Li Intermetallic Layer for Stable Cycling of All-Solid-State Lithium Batteries. *Adv. Sci.* **2022**, *9*, 2103826.

(40) Luo, S.; Zhang, Y.; Liu, X.; Wang, Z.; Fan, A.; Wang, H.; Ma, W.; Zhu, L.; Zhang, X. Thermal Behavior of Li Electrode in All-Solid-State Batteries and Improved Performance by Temperature Modulation. *Int. J. Heat Mass Transfer* **2022**, *199*, 123450.